Supporting Information

Cooperative Effects between Hydrophilic Pores and Solvents: Catalytic Consequences of Hydrogen Bonding on Alkene Epoxidation in Zeolites

Daniel T. Bregante,[1] Alayna M. Johnson,[1] Ami Y. Patel,[1] E. Zeynep Ayla,[1] Michael J. Cordon,[2] Brandon C. Bukowski,[2] Jeffrey Greeley,[2] Rajamani Gounder,[2] and David W. Flaherty[1,*]

[1]Department of Chemical and Biomolecular Engineering, University of Illinois at Urbana-Champaign, Urbana, Illinois 61801, United States

[2]Charles D. Davidson School of Chemical Engineering, Purdue University, West Lafayette, Indiana 60208, United States

*Corresponding Author

Phone: (217) 244-2816

Email: dwflhrty@illinois.edu

S1.0 Additional Catalyst Characterization

S1.1 Catalyst Characterization

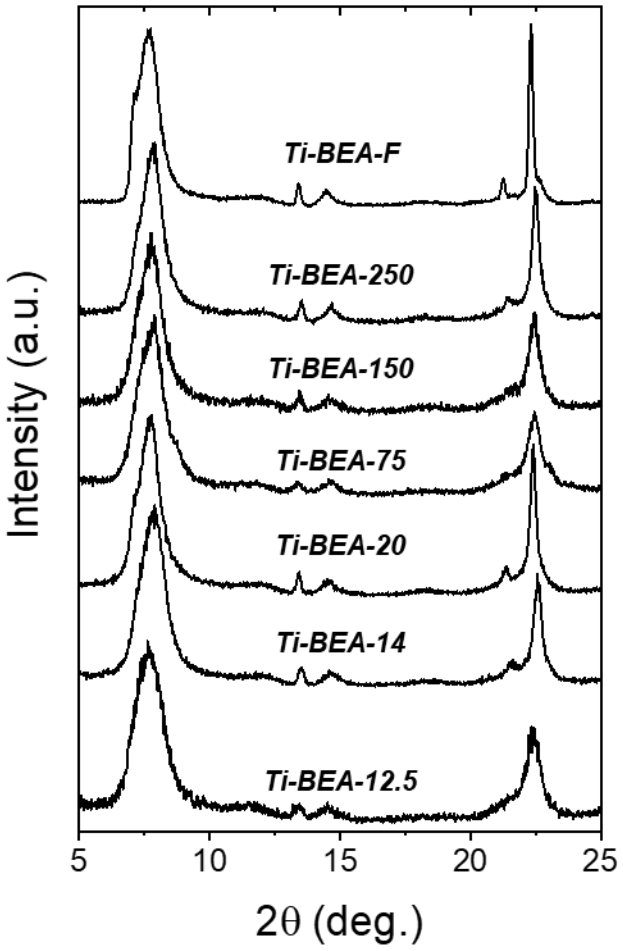

Figure S1. X-ray diffractograms for all Ti-BEA used within this study. Diffractograms are vertically offset for clarity.

Figure S1 shows X-ray diffractograms for all Ti-BEA contain distinct crystallographic features that are indicative of the *BEA framework. Notably, the sharpness in the ~22.4 deggree XRD feature for Ti-BEA-F is indicative of a high-degree of crystallinity, which is expected for Ti-BEA that is synthesized in fluoride media. All other Ti-BEA contain broader features that are indicative of internal defects that form upon dealumination and synthesis in hydroxide media.

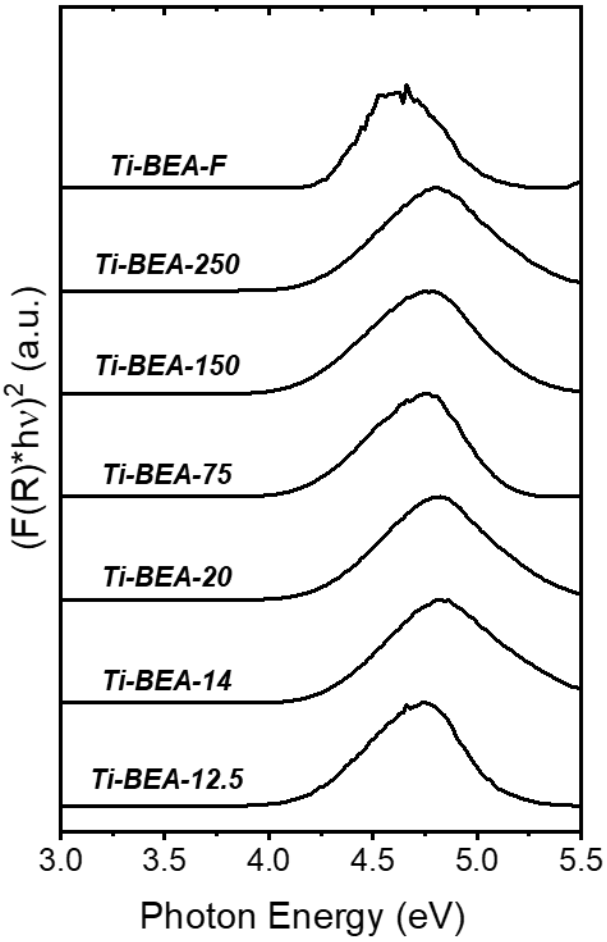

Figure S2. Tauc plots for all Ti-BEA used within this study. Diffuse-reflectance UV-vis spectra were collected under ambient conditions (~298 K). Ti-BEA were dehydrated in flowing air (100 cm^{-1} min^{-1}) for 6 h at 823 K prior to measurement. Tauc plots are normalized to the intensity of the feature at ~4.6 eV and are vertically offset for clarity.

Figure S2 shows that all Ti-BEA used within this study contain a single UV-vis absorbance feature around 4.6 eV. The leading edge (~4.2 – 4.5 eV) was fit using a line to extrapolate the x-intercept, which corresponds to the band gap of the materials. In all cases, the band gap (4.2 – 4.3 eV, Table 1) is significantly higher than that of bulk TiO_2 (~3.2 eV), which suggests that all Ti-BEA contain Ti atoms that are highly disperse and does not contain spectroscopically-observable fractions of bulk or oligomeric TiO_2.

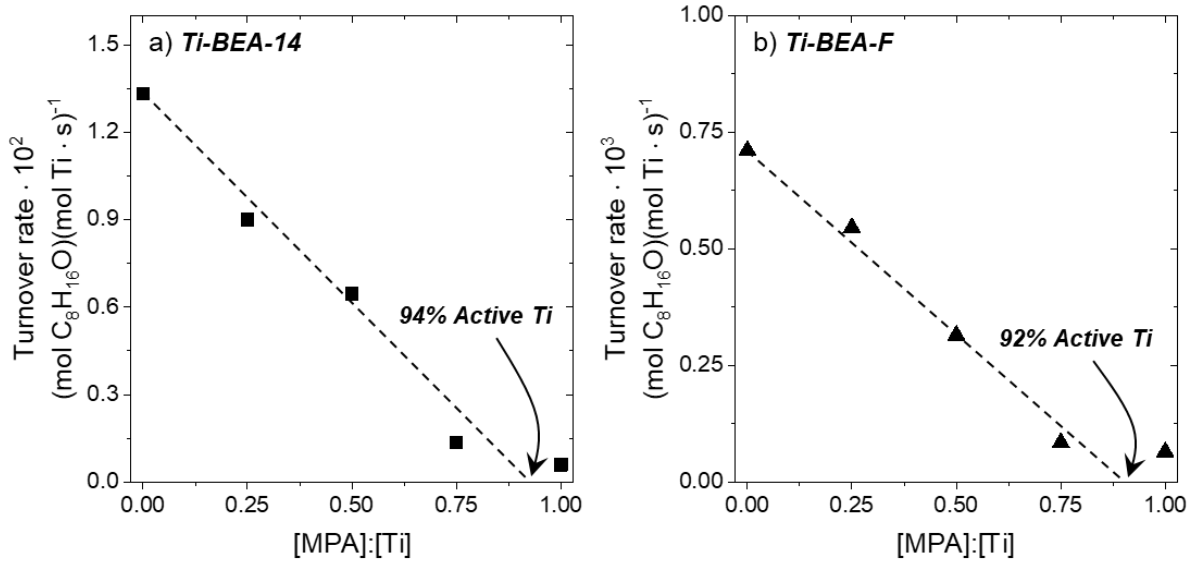

Figure S3. Turnover rates for $C_8H_{16}O$ formation as a function of methylphosphonic acid to Ti ratio ([MPA]:[Ti]; 0.01 M C_8H_{16}, 0.01 M H_2O_2) over (a) Ti-BEA-14 and (b) Ti-BEA-F. The dashed lines represent linear regression fits with the y-intercept set to the turnover rate in the absence of the MPA titrant.

Figure S3 shows representative plots for the turnover rate of C_8H_{16} epoxidation as a function of the ratio of MPA titrant to Ti atoms within Ti-BEA. For all Ti-BEA, the turnover rates for epoxidation decrease linearly with [MPA]:[Ti], which suggests that all active sites are catalytically equivalent within a given Ti-BEA. The x-axis intercept, where the turnover rates are extrapolated to zero is used as the amount of *active* Ti in each Ti-BEA for the epoxidation kinetics in section 3.4.

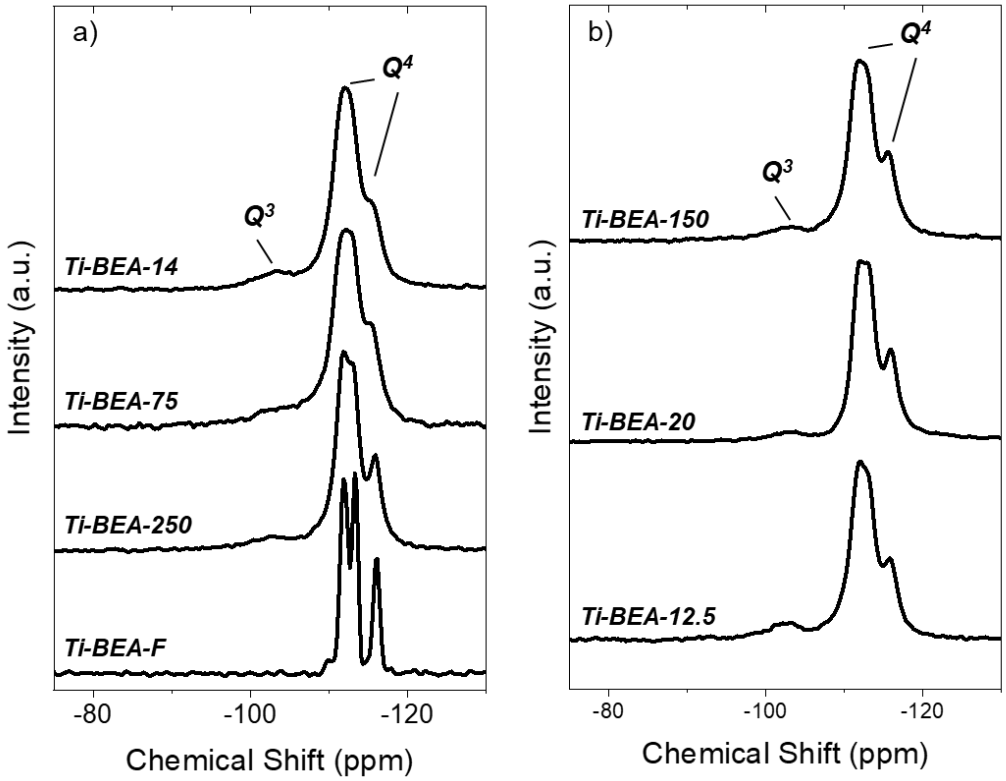

Figure S4. ^{29}Si direct polarization MAS-NMR of (a) Ti-BEA-14, Ti-BEA-75, Ti-BEA-250, and Ti-BEA-F and (b) Ti-BEA-12.5, Ti-BEA-20, and Ti-BEA-150. Spectra were obtained at ambient conditions (~298 K). Ti-BEA-X were dehydrated in flowing air (100 cm^3 min^{-1}) for 6 h at 823 K prior to measurement. Spectra are vertically offset for clarity.

Figure S4 shows ^{29}Si MAS-NMR spectra of all Ti-BEA contain distinct features at at -102 ppm and between 112 and 116 ppm, which correspond to Q^3 (i.e., $Si(OH)(OSi)_3$) and Q^4 (i.e. $Si(OSi)_4$) forms of Si atoms, respectively. The integrated area for the Q^3 sites relative to all ^{29}Si MAS-NMR features yields the fraction of Si atoms that possess a single hydroxyl moiety. The fraction of Q^3 (i.e., Φ_{NMR}) increases with the "hydrophilicity" of the materials. Notably, Ti-BEA-F does not contain any significant fraction of Q^3 sites, as this material was synthesized with the intention of creating a nearly defect-free pore structure. The splitting of the Q^4 sites (e.g., Ti-BEA-F, Ti-BEA-250) is indicative of a highly crystalline material, where this splitting represents contributions from the various crystallographically-distinct Si atoms within the BEA framework.

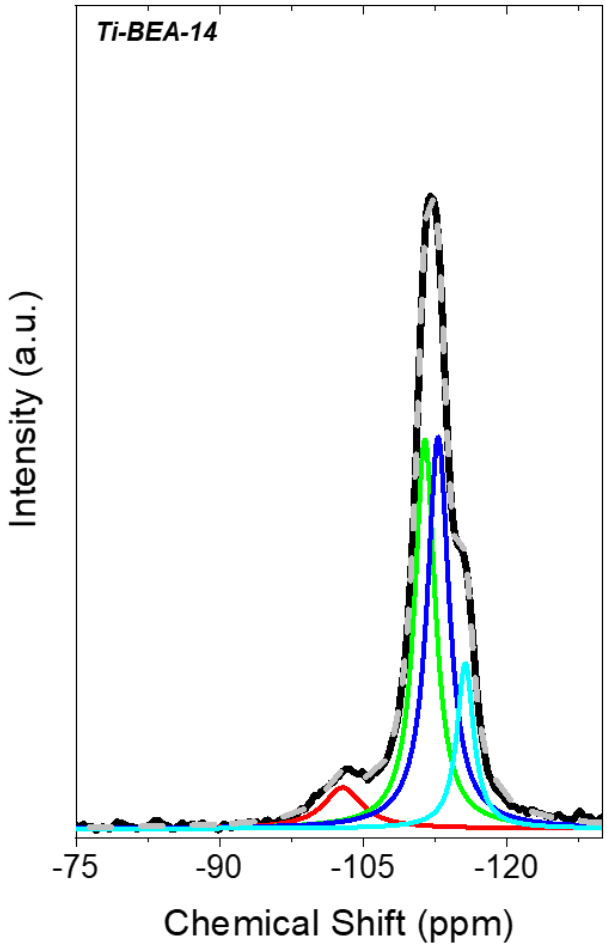

Figure S5. Example peak fitting procedure for ^{29}Si direct polarization MAS-NMR of Ti-BEA-12.5. The red curve represents NMR features attributed to Q^3 sites, while green, blue, and teal curves correspond to Q^4 sites; the gray curve represents the cumulative fit. Lorentzian curves were used for fitting procedure. Φ_{NMR} was estimated by dividing the area under the red curve by that of the gray curve.

Figure S5 shows an example peak-fitting procedure to quantify values of Φ_{NMR}. The red, green, blue, and teal peaks were fit with peak centers constrained at -102, -112, -113, and -116 ppm, based upon literature precedent for Q^3 sites[1-2] and the normal-splitting pattern of Q^4 sites.[3]

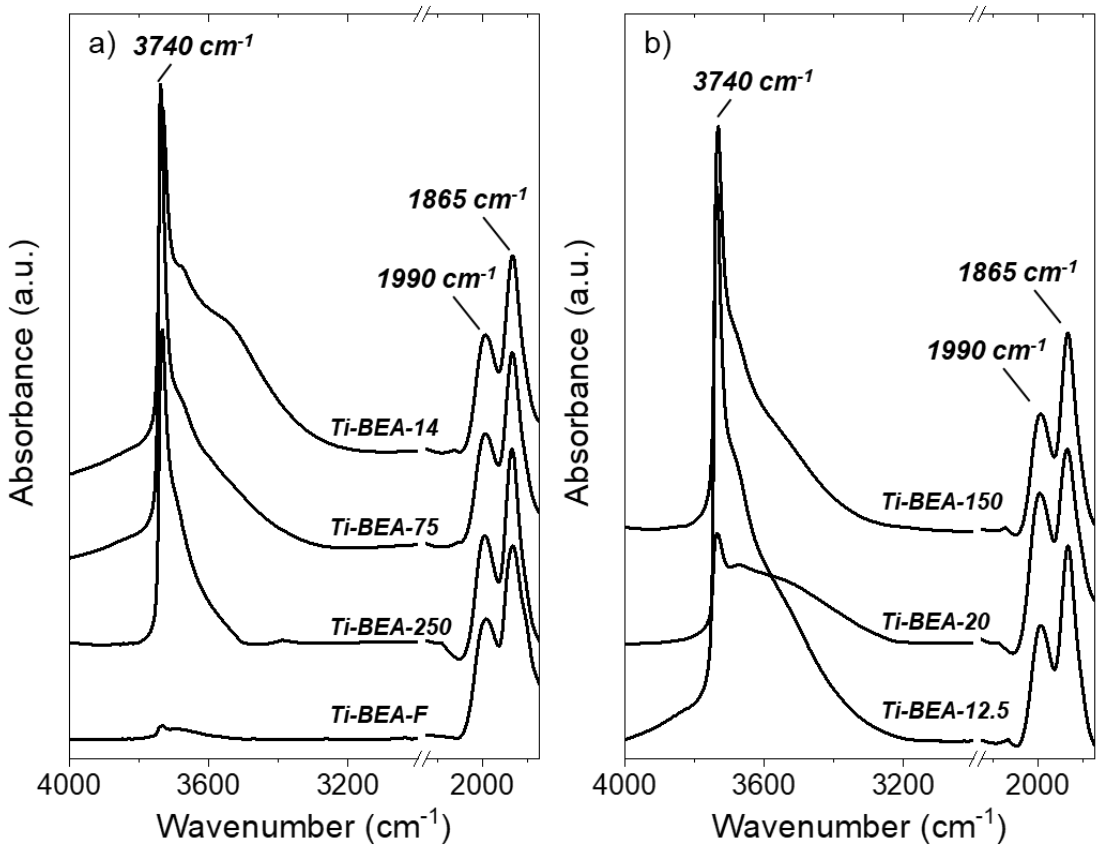

Figure S6. Infrared spectra of dehydrated (a) Ti-BEA-14, Ti-BEA-75, Ti-BEA-250, and Ti-BEA-F, and (b) Ti-BEA-12.5, Ti-BEA-20, and Ti-BEA-150. All Ti-BEA were dehydrated *in situ* under flowing He (50 cm^3 min^{-1}) for >2 h at 573 K prior to measurement. All spectra were normalized to an absorbance feature at 1865 cm^{-1} corresponding to ν(Si-O-Si) overtones (1865 and 1990 cm^{-1}), which is used as an internal standard for comparisons between the density of SiOH groups among Ti-BEA samples. Spectra are vertically offset for clarity.

Figure S6 shows the ν(O-H) and ν(Si-O-Si) overtone region of the infrared spectra of dehydrated Ti-BEA. The sharp absorbance feature at ~3740 cm^{-1} corresponds to isolated SiOH species that are not interacting via H-bonding with nearby H-bond donors or acceptors (i.e., other SiOH). The broadening within the ν(O-H) region is due to the H-bonding interactions of SiOH with other SiOH (i.e., $(SiOH)_4$) that cause a red shift in these vibrational modes.

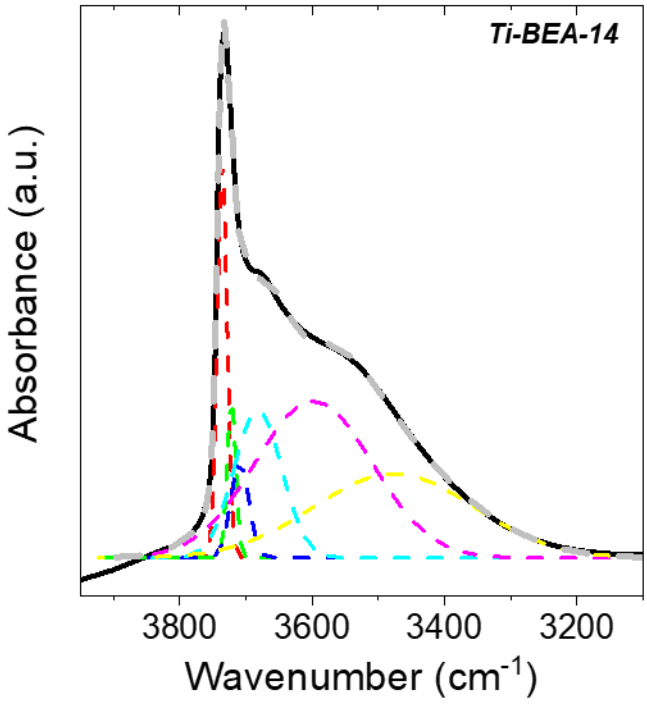

Figure S7. Infrared spectra of dehydrated Ti-BEA-14 that was treated in flowing He (50 cm^3 min^{-1}) for >2 h at 573 K prior to measurement. Gaussian curves were fit to the infrared spectra. Gray dashed curve represents cumulative fit of the six colored curves.

Six gaussian curves were chosen to peak fit the infrared spectra of dehydrated Ti-BEA so as to capture the curvature of the spectra and yield a R^2 value >0.995. Peak fits using three, four, and five curves were attempted and gave nearly identical results (i.e., values of Φ_{IR}). As such, six curves were chosen to fit all Ti-BEA to calculate values of Φ_{IR} (Table 1) and gave R^2 >0.995 in all cases.

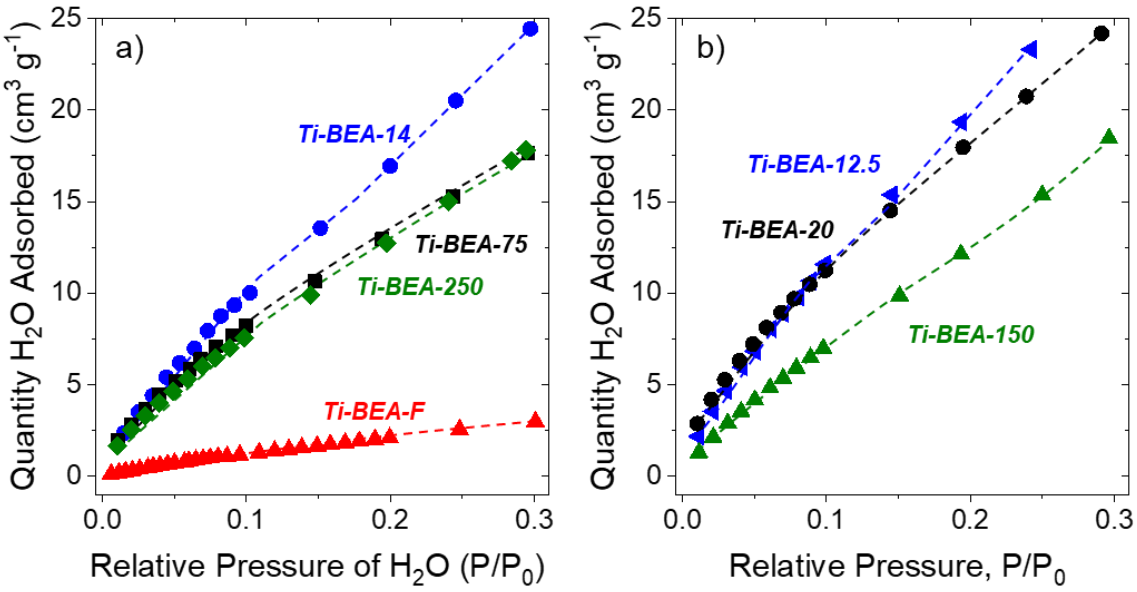

Figure S8. H_2O adsorption isotherms for (a) Ti-BEA-14 (blue ▼), Ti-BEA-75 (black ■), Ti-BEA-250 (orange ♦), and Ti-BEA-F (red ►) and (b) Ti-BEA-12.5 (blue ▼), Ti-BEA-20 (black ●), and Ti-BEA-150 (green ▲) at 293 K. All Ti-BEA were degassed under vacuum ($<7 \cdot 10^{-4}$ kPa, 673 K) for 6 h prior to measurement. Dashed curves are intended to guide the eye.

Figure S8 shows H_2O uptake within Ti-BEA-F is much lower than all Ti-BEA synthesized by post-synthetic modification for $P/P_0 < 0.3$. This is because SiOH and $(SiOH)_4$ nucleate H_2O cluster formation, which precludes measureable differences in the uptake of H_2O among Ti-BEA that contain significant amounts of $(SiOH)_4$ (i.e., those synthesized by post-synthetic modification).

S2.0 Adsorption of CD_3CN onto Lewis Acidic Ti atoms, SiOH sites, and Pore Walls
S2.1 Peak Fitting of Infrared Spectra of CD_3CN Adsorbed to Ti-BEA-12.5 and van't Hoff Analysis

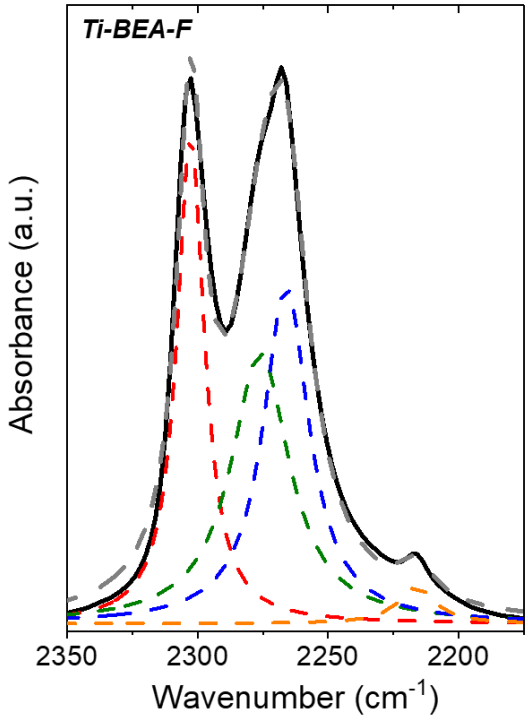

Figure S9. Example peak fitting of infrared spectra of CD_3CN adsorbed on Ti-BEA-F (2.4 kPa CD_3CN, 50 cm^3 min^{-1} He, 387 K). Color key: $\nu(C\equiv N)$ of CD_3CN coordinated to Ti atoms (red), SiOH atoms (green), and *BEA pore walls (blue); $\nu_{as}(CD_3)$ (orange); cumulative fit (gray). Lorentzian curves were used for the fitting procedure.

Figure S9 shows a representative peak-fitting procedure used to determine the areas of $\nu(C\equiv N)$ for CD_3CN bound to different types of adsorption sites (i.e., Ti, SiOH, and *BEA pore walls). Lorentzian curves were chosen, because gaussian fits (i.e., those used for Φ_{IR} analysis) did not yield R^2 values >0.98 when fitting the data. When fitting subsequent spectra (e.g., during the CD_3CN adsorption isotherm or isobar) the peak centers were fixed at 2302, 2274, 2263, and 2215 cm^{-1} for $\nu(C\equiv N)$ of CD_3CN coordinated to Ti atoms, SiOH atoms, and *BEA pore walls, and $\nu_{as}(CD_3)$, respectively.

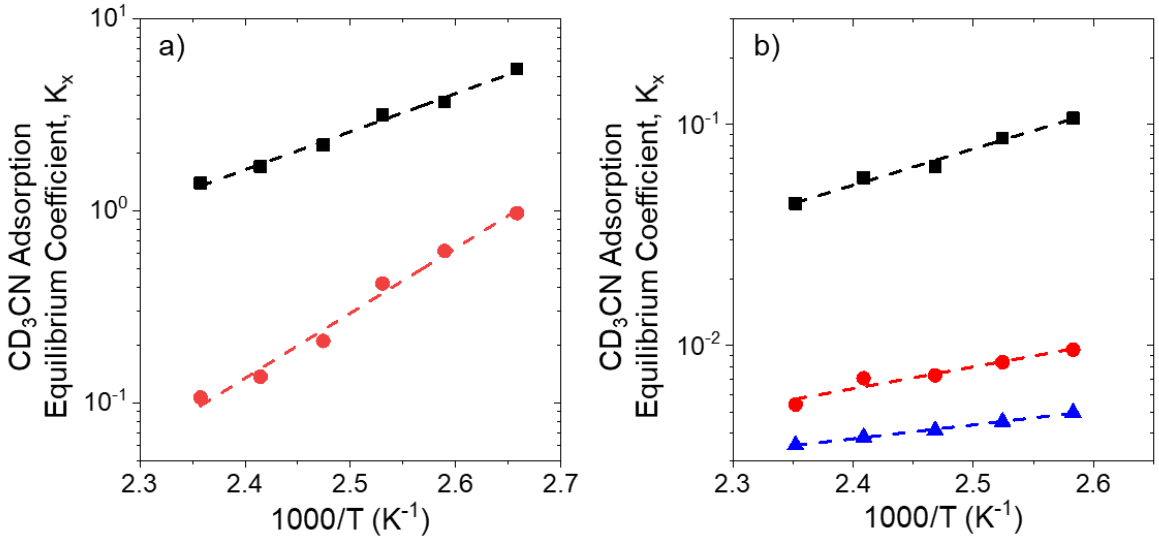

Figure S10. Equilibrium constants for the adsorption of CD_3CN to Ti atoms (black ■; ~2302 cm^{-1}), SiOH groups (red ●; ~2274 cm^{-1}), and *BEA pore walls (blue ▲; ~2263 cm^{-1}) as a function of inverse temperature for (a) Ti-BEA-12.5, and for (b) Ti-BEA-F (0.46 kPa CD_3CN, ~101 kPa He, 373 – 423 K). Dashed lines represent fits of equation 6, whose slope and intercept are proportional to $\Delta H_{CD_3CN,x}$ and $\Delta S_{CD_3CN,x}$, respectively.

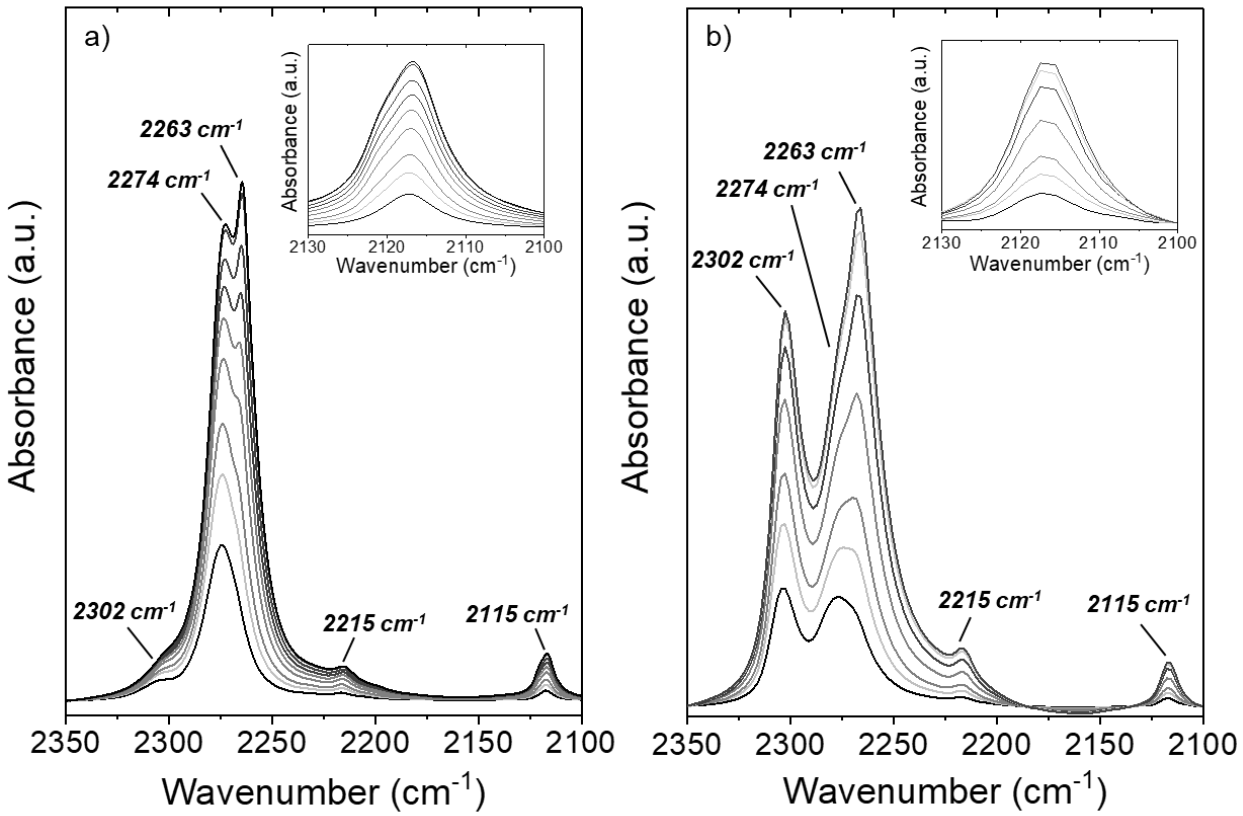

Figure S11. Infrared spectra of equilibrium coverages of adsorbed CD_3CN on (a) Ti-BEA-12.5 (0.46 – 6.95 kPa CD_3CN, 346 K), and (b) Ti-BEA-F (0.46 – 5.03 kPa CD_3CN, 387 K). The inset shows zoomed-in regions to clearly observe $\nu_s(CD_3)$.

Figure S11 shows infrared spectra of Ti-BEA-12.5 and Ti-BEA-F obtained *in situ* while contacting the catalysts with He streams containing CD_3CN. The insets of Figure S11 shows a zoomed-in region to clearly observe $\nu_s(CD_3)$, where there is clearly an overlapping feature that is blue shifted (i.e., to higher wavenumbers) on Ti-BEA-12.5 with increasing partial pressure of CD_3CN. The $\nu_s(CD_3)$ region on Ti-BEA-F, however, appears to be symmetric at all partial pressures of CD_3CN. Ti-BEA-12.5 contains silanols predominantly in the form of $(SiOH)_4$, which Ti-BEA-F contains silanols that are most-likely isolated and formed stochastically during crystallization. This suggests that as the partial pressure of CD_3CN is increased and the coverage over $(SiOH)_4$ on Ti-BEA-12.5 is increased, $\nu_s(CD_3)$ blue shifts as a result of the interaction between CD_3CN and $(SiOH)_4$. The interaction of the $-CD_3$ moiety with a Lewis basic function is known to cause a blue shift in $\delta_s(-CD_3)$,[4] while the interaction between a Lewis acid and the nitrile function (e.g., $Ti–NCCD_3$) does not affect $\nu_s(-CD_3)$.[5] This suggests that the electropositive end of CD_3CN (i.e., $-CD_3$) is surrounded by an electronegative environment (e.g., interactions with the silanol nest).

S2.3 Adsorption Entropies Estimated by Campbell *et al.'s* Model

Adsorption onto solid surfaces result in losses of entropy with respect to the gas-phase species, which primarily correspond to losses in translational and rotational forms of entropy. Campbell et al. have shown that the standard state entropies of adsorbed species ($S^0_{ads}(T)$) can be estimated to be proportional to the entropy of the gas-phase molecule[6] ($S^0_{gas}(T)$) by the relationship

$$S^0_{ads}(T) = 0.7 \cdot S^0_{gas}(T) - 3.3 \cdot R \quad \text{(S1)}$$

where T is the absolute temperature and R is the ideal gas constant. The standard entropy of gaseous CD_3CN at 350 K is near 257 J mol^{-1} K^{-1} (approximated from tabulated data for CH_3CN),[7] which suggests an entropic loss upon adsorption of ~114 J mol^{-1} K^{-1} based on equation S7 and the difference between values of $S^0_{gas}(T)$ and $S^0_{ads}(T)$. This estimate further suggests that the measured loss of entropy due to adsorption of CD_3CN onto $(SiOH)_4$ within Ti-BEA-12.5 (-150 ± 10 J mol^{-1} K^{-1}, Table 3) must result from additional interactions between CD_3CN and $(SiOH)_4$ that further constrain motion of this molecule upon adsorption to $(SiOH)_4$ nests.[6]

S2.3 Partition Functions and Entropy Estimates for CD_3CN Molecules Bound to Ti and $(SiOH)_4$ Sites.

The two main contributors of vibrational entropy for CD_3CN molecules bound to Lewis acidic Ti atoms sites and $(SiOH)_4$ groups are frustrated translational and hindered rotational modes.

The partition function used to describe frustrated translation ($q_{F,trans}$) for a bound surface species is given by

$$q_{F,trans} = \frac{e^{\left(\frac{-h\nu_{trans}}{2k_BT}\right)}}{1-e^{\left(\frac{-h\nu_{trans}}{2k_BT}\right)}} \quad \text{(S2)}$$

where h and k_B are Planck's and Boltzmann's constants, respectively, and ν_{trans} is the frequency for the frustrated translational vibration of the adsorbate,[8] which is modelled as a harmonic oscillation. The frequency of the vibration is calculated using
the relathionship

$$\nu_{trans} = \left(\frac{E_d}{2md_m{}^2}\right)^{1/2} \quad \text{(S3)}$$

where the depth of the potential (E_d) is taken to be the difference in enthalpy between CD_3CN at the adsorption site (i.e., Ti atom or $(SiOH)_4$ group) and CD_3CN physisorbed to the pore wall. This treatment provides a lower bound for the barrier to move CD_3CN from one site to the pore wall and subsequently to a distinct Ti atom or $(SiOH)_4$ group. The distance between sites (d_m; i.e., width of the energy well for frustrated translational movement) is approximated here as 4 Å and 1 Å for Lewis acidic Ti sites for SiOH sites, respectively). The mass (m) is that of the coordinated complex.

The two-dimensional hindered rotation partition function ($q_{H,rot}$) describes the rotation of a quasi-linear adsorbate (e.g., CD_3CN bound to Ti atoms) that resembles a cone in three-dimensional space.[9] This motion is represented by

$$q_{H,rot} = \left(\frac{4\pi^2 k_B T I_r}{\sigma^2 h^2}\right)^{1/2} e^{\left(\frac{-V_0}{2k_BT}\right)} J_0\left(\frac{iV_0}{2k_BT}\right) \quad \text{(S4)}$$

where σ is the periodicity of hindered rotation, assumed to be 40 degrees, I_r is the moment of rotational inertia

$$I_r = \sum_{i=1}^{l} m_i r_i^2 \quad \text{(S5)}$$

reflected by the mass (m_i) and distance (r_i) of each atom (i.e., N, C, and D; estimated from structural properties of CH_3CN)[10-11] from the center of rotation (i.e., the N atom), V_o is the rotational barrier height

$$V_0 = \frac{8\pi^2 \nu^2 I_r}{\sigma^2} \quad \text{(S6)}$$

where the vibrational frequency (ν) between the two adsorbing atoms (i.e., N and Ti; was estimated as 180 cm^{-1} based upon infrared spectra of CH_3CN bound to various transition-metal complexes),[12] and $J_0(x)$ is the Bessel's function of the first kind. The N atoms was chosen as the center of rotation in equation S5 to avoid overestimating the entropic contributions from hindered rotation that may overlap with frustrated translation. Partition functions describing both frustrated translational and hindered rotational modes (q_x) are related to entropies (S_x) by the Sackur-Tetrode equation[8]

$$S_x = Rln(q_x) + RT\left[\frac{\partial \ln(q_x)}{\partial T}\right] \quad \text{(S7)}$$

where x denotes the specific vibrational mode.

Equations S2, S4, and S7 allow for estimation of the entropic contributions resulting from frustrated translation and hindered rotation of CD_3CN molecules adsorbed on Ti and $(SiOH)_4$ sites. CD_3CN bound to $(SiOH)_4$ possess negligible contributions from hindered rotation, as these adsorption into these SiOH nests results in the loss of all three-dimensions of rotational entropy. Therefore, adsorption of CD_3CN onto $(SiOH)_4$ and Ti active sites (shown visually in Figure S12) are contain vibrational modes derived from frustrated translation, while the latter contains also contributions from hindered rotation. The entropies for CD_3CN bound to Ti and $(SiOH)_4$ sites (Table 1) are estimated, using the above analysis, to be 95 and 29 J mol^{-1} K^{-1}, respectively.

Table S1. Entropy Estimates for CD_3CN bound to $(SiOH)_4$ and Ti atoms at 350 K.

AdsorptionSite	S_{trans} (J mol^{-1} K^{-1})	S_{rot} (J mol^{-1} K^{-1})	S_{trans} + S_{rot} (J mol^{-1} K^{-1})
Ti[a]	57	38	95
$(SiOH)_4$[a]	29	--	29
Si-O-Si[b]	120	135	255
Ti[b]	123	123	246
$(SiOH)_4$ (single CD_3CN)[b]	112	96	208
$(SiOH)_4$ (three CD_3CN)[b]	113	75	188

[a]Calculated using the Sackur-Tetrode equation. [b]Calculated by decomposing the transitional and rotational contributions of entropy from the DFT model. We note the large translational and rotational entropies predicted by the DFT model. We hypothesize there are due to the difficulty in exhaustively sampling all modes in a gas phase adsorbate, and instead focus on the relative change in translational and rotational entropies when adsorbed in Ti and $(SiOH)_4$.

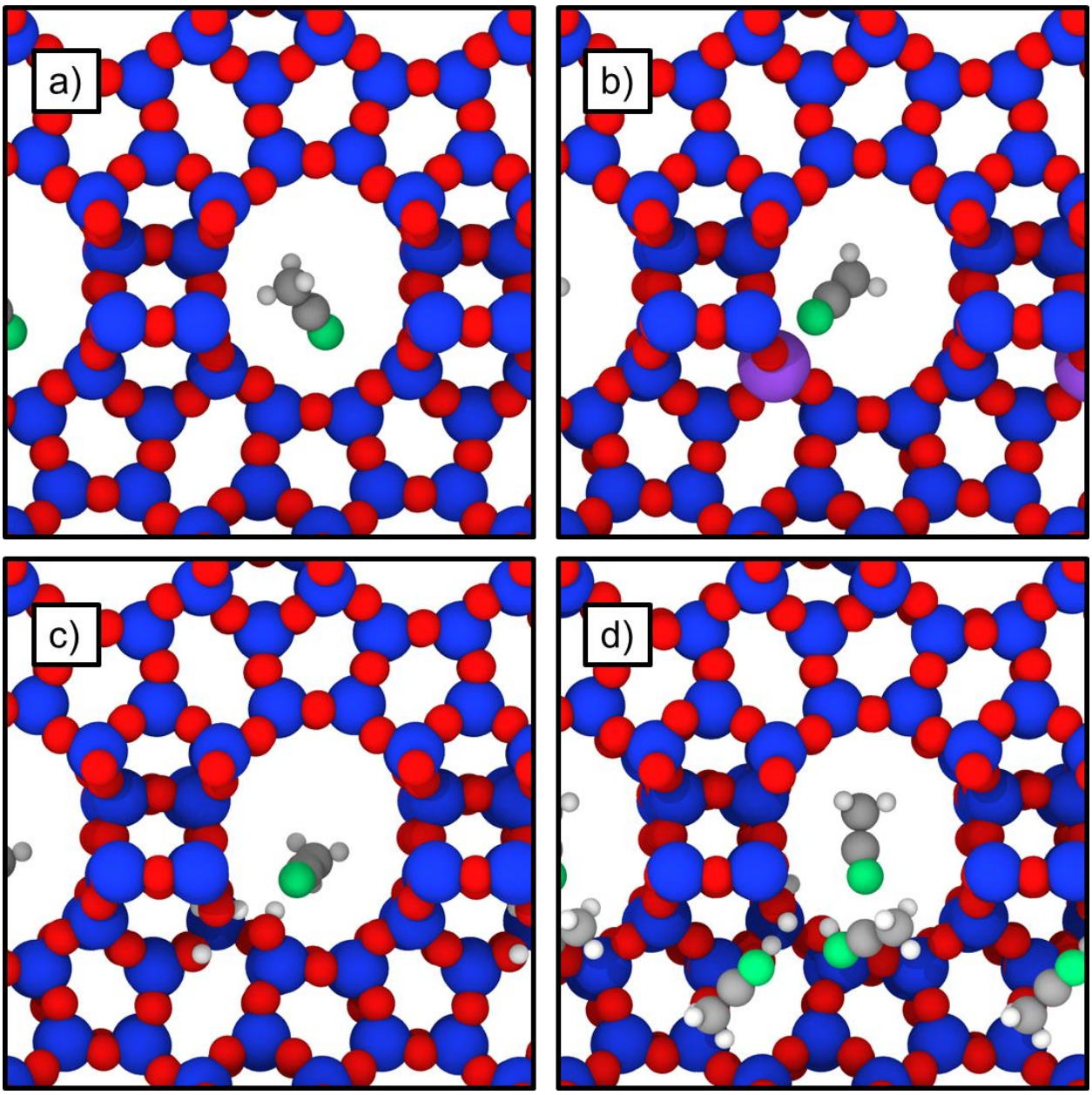

Figure S12. Representitive geometries from AIMD of interactions between a single CD_3CN adsorbed onto (a) Si-O-Si, (b) Ti, and (c) $(SiOH)_4$. Figure S12d represents the adsorption of three CD_3CN onto $(SiOH)_4$, where the CD_3CN on the bottom-left corner of the figure is interacting with the small side channel resulting from the vacancy within $(SiOH)_4$. Color scheme for atoms: hydrogen (white), carbon (gray), nitrogen (green), oxygen (red), silicon (blue), titanium (purple).

S3.0 *In Situ* UV-vis Spectra of Ti-BEA Contacted with Solutions of H_2O_2

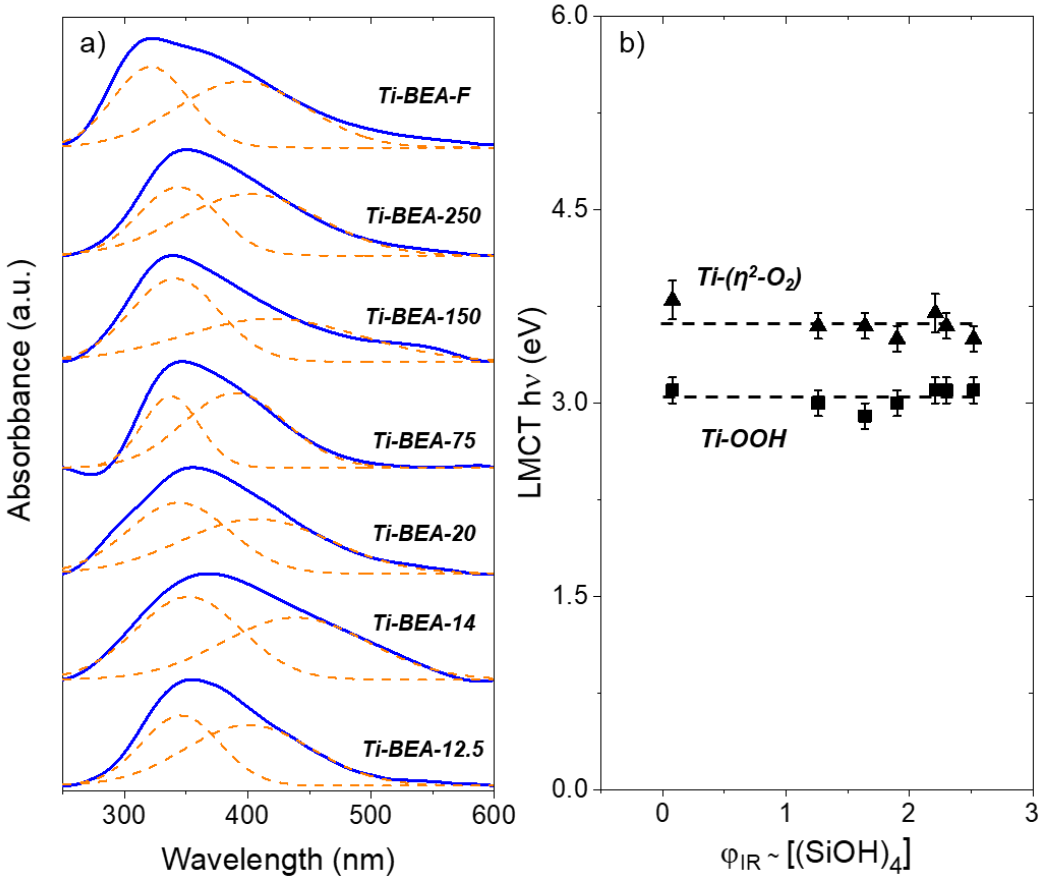

Figure S13. (a) UV-vis spectra of Ti-BEA obtained *in situ* under conditions that result in Ti-(η^2-O_2) (blue) and Ti-OOH (orange) saturated surfaces (0.01 M H_2O_2 in CH_3CN, 313 K; Section 3.4) and (b) ligand-to-metal charge transfer energies (LMCT hν) of Ti-OOH (■) and Ti-(η^2-O_2) (▲) species as a function of Φ_{IR}. Dashed curves in Figure S13a represents gaussian fits to UV-vis absorbance features and dashed lines in Figure S13b are intended to guide the eye. Spectra are normalized by their maximum absorbance and vertically offset for clarity.

Figure S13a shows UV-vis spectra obtained *in situ* when contacting Ti-BEA with solutions of H_2O_2 to visualize the absorbance features that form upon activation of H_2O_2. In all cases, the broad UV-vis feature (300 – 500 nm) contains two overlapping gaussian peaks that correspond to titanium hydroperoxo (Ti-OOH; higher wavelengths, lower energies) and peroxo (Ti-(η^2-O_2); lower wavelengths, higher energies) species. Figure S13b shows the ligand-to-metal charge transfer energies for Ti-OOH and Ti-(η^2-O_2) do not vary with Φ_{IR}, which suggests that the presence, proximity, and density of $(SiOH)_4$ within Ti-BEA do not significantly affect the electronic properties of the reactive species that form upon H_2O_2 activation.

S4.0 Additional Kinetic Data and Derivation of Rate Expression for H_2O_2 Decomposition

S4.1 C_8H_{16} Epoxidation Rates as a Function of [C_8H_{16}], [H_2O_2], and [H_2O] on Ti-BEA.

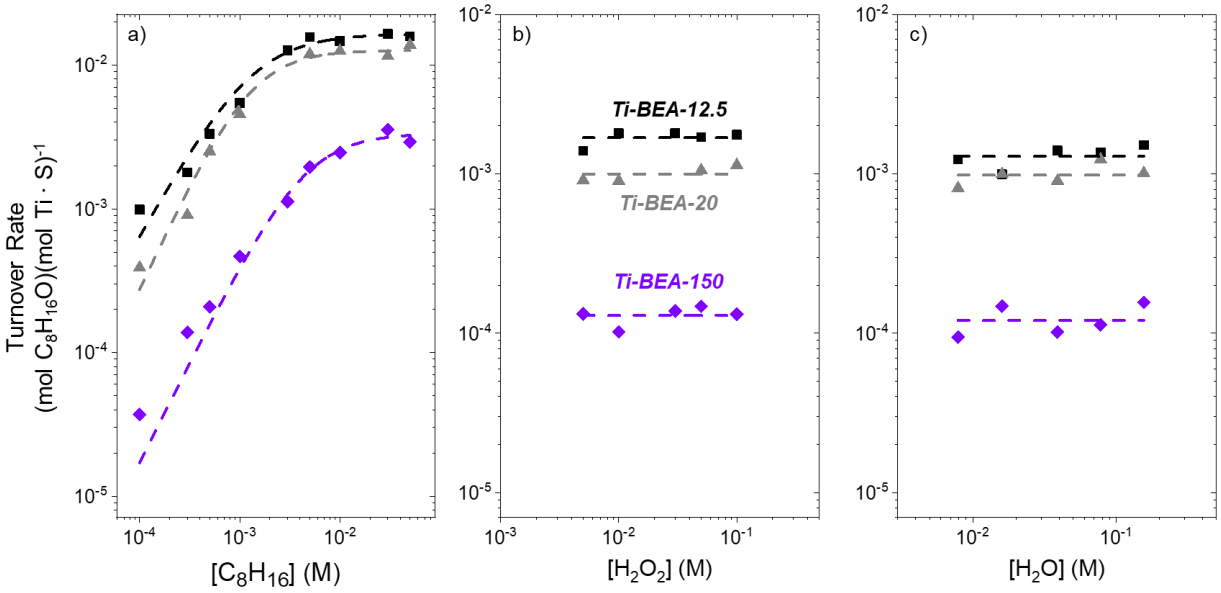

Figure S14. Turnover rates for the formation of $C_8H_{16}O$ as a function of the concentrations of (a) C_8H_{16} (0.01 M H_2O_2, 0.039 M H_2O), (b) H_2O_2 ($3 \cdot 10^{-4}$ M C_8H_{16}), and (c) H_2O ($3 \cdot 10^{-4}$ M C_8H_{16}, 0.01 M H_2O_2) on Ti-BEA-12.5 (black ■), Ti-BEA-20 (gray ▲), and Ti-BEA-150 (purple ♦) in CH_3CN at 313 K. Dashed lines represent least-squares regression fits of equation 8 (Figure S13a) and 11 (Figures S13b and S13c).

S4.2 Derivation of the Rate Expression for H_2O_2 Decomposition

Scheme 1. Proposed Elementary Steps for C_8H_{16} Epoxidation and H_2O_2 Decomposition over Ti-BEA[a]

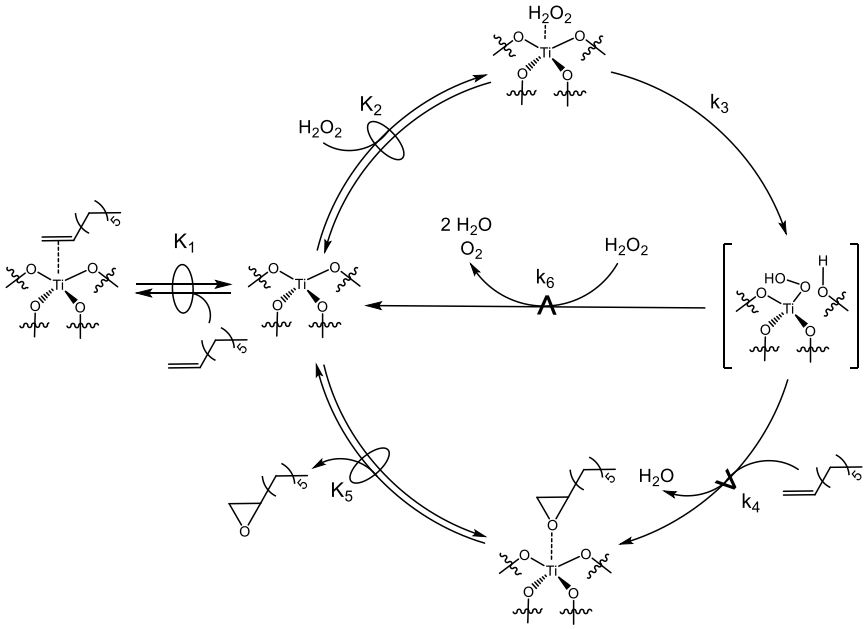

[a]The symbol ⇄ represents a quasi-equilibrated step, while → represents a kinetically relevant step. The Ti-OOH intermediate drawn are intended to represent the pool of Ti-OOH and Ti-(η^2-O_2) species that are present as shown by UV-vis (Figure 5).

Scheme 1 depicts a series of elementary steps that describe the measured effects of [C_8H_{16}], [H_2O_2], and [H_2O] on the rates of H_2O_2 decomposition. This catalytic cycle involves the quasi-equilibrated adsorption of C_8H_{16} (step 1) and H_2O_2 (step 2), and the irreversible activation of adsorbed H_2O_2 (step 3) to form Ti-(η^2-O_2) and Ti-OOH intermediates. Ti-OOH species (Section 3.3) then react with C_8H_{16} (step 4) or H_2O_2 (step 6) both of which react either from the fluid-phase directly (i.e., via an Eley-Rideal mechanism) or following coordination to a distinct site at which H_2O_2 does not activate (e.g., the pore wall or SiOH). These pathways form $C_8H_{16}O$, which then desorbs (step 5), or decomposition products (e.g., O_2 and H_2O), respectively. The reaction between Ti-OOH and H_2O_2 is kinetically relevant, which leads to rate for H_2O_2 decomposition (r_D)

$$r_D = k_6[H_2O_2][Ti-OOH] \tag{S8}$$

where [Ti-OOH] is the number of Ti-OOH intermediates and k_i is the rate constant for step "i" in Scheme 1. The application of the pseudo-steady state hypothesis on Ti-OOH and a site balance over all possible states of the Ti active site allows equation S8 to be restated as

$$\frac{r_D}{[L]} = \frac{\frac{k_3 k_6 K_2 [H_2O_2]^2}{k_4[C_8H_{16}]+k_6[H_2O_2]}}{1+K_1[C_8H_{16}]+K_2[H_2O_2]+\frac{k_3 K_2[H_2O_2]}{k_4[C_8H_{16}]+k_6[H_2O_2]}+\frac{1}{K_5}[C_8H_{16}O]} \quad \text{(S9)}$$

where [L] is the total number of active sites and K_i is the equilibrium constant for step "i." The five terms in the denominator correspond to active metal atoms occupied by CH_3CN (i.e., the solvent), C_8H_{16}, H_2O_2, Ti-OOH, or $C_8H_{16}O$, respectively.

Reaction conditions that result in epoxidation turnover rates that are proportional to $[C_8H_{16}]$ and invariant with $[H_2O_2]$, result in surfaces that are saturated with Ti-OOH intermediates.[13-16] When Ti-OOH is assumed to be the most abundant reactive intermediate (MARI), the term in the denominator of equation S9 that corresponds to the coverage of this surface species (i.e., the fourth term) dominates and yields a rate expression of the form

$$\frac{r_D}{[L]} = k_6[H_2O_2] \quad \text{(S10)}$$

S4.3 Temperature Dependence of C_8H_{16} Epoxidation and H_2O_2 Decomposition Rates

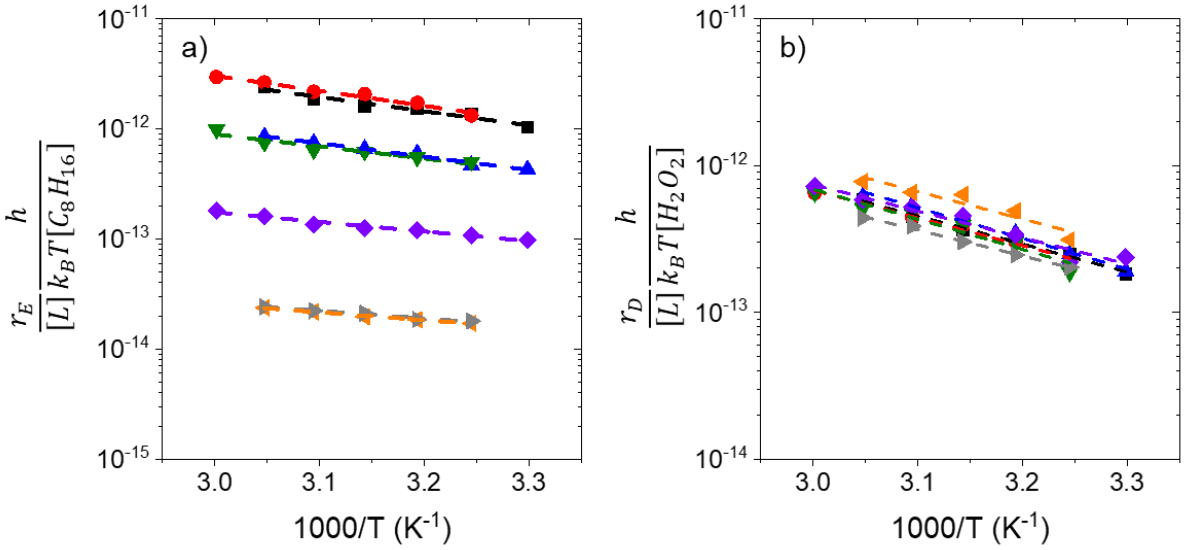

Figure S15. Turnover rates for (a) C_8H_{16} epoxidation and (b) H_2O_2 decomposition divided by $\frac{k_BT}{h}[C_8H_{16}]$ or $\frac{k_BT}{h}[H_2O_2]$ as a function of inverse temperature for Ti-BEA (0.1 mM C_8H_{16}, 0.01 M H_2O_2, in CH_3CN). Symbol key: Ti-BEA-12.5 (black ■); Ti-BEA-14 (red ●); Ti-BEA-20 (blue ▲); Ti-BEA-75 (green ▼); Ti-BEA-150 (purple ♦); Ti-BEA-250 (orange ◀); Ti-BEA-F (gray ▶). Dashed lines represent fit of equations 14a and 14b, whose slopes are proportional to $\Delta H_{E,App}^{\ddagger}$ and $\Delta H_{D,App}^{\ddagger}$, and intercepts are proportional to $\Delta S_{E,App}^{\ddagger}$ and $\Delta S_{D,App}^{\ddagger}$, respectively.

S5.0 Equilibrium Adsorption of C_8H_{16} onto Ti-BEA

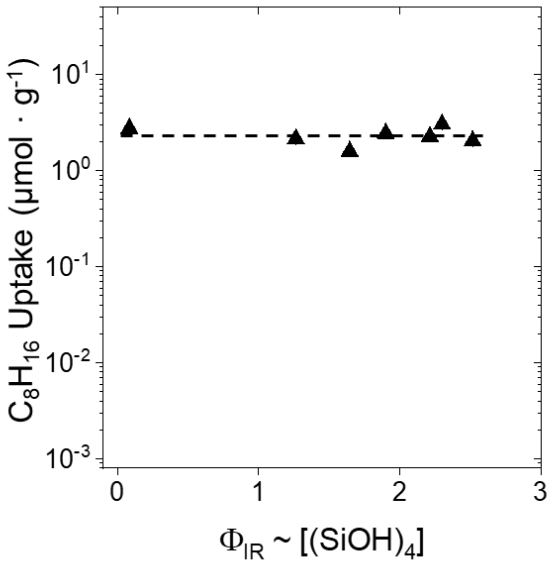

Figure S16. Uptake of C_8H_{16} into Ti-BEA as a function of Φ_{IR} in CH_3CN (0.1 mM C_8H_{16}, 0.039 M H_2O, 313 K). The span of the y-axis was chosen to facilitate comparisons with Figures 7a and 8. Dashed line is intended to guide the eye.

Figure S16 shows the uptake of C_8H_{16} into Ti-BEA under conditions that mimic the reaction solution (in the absence of H_2O_2), where the amount of C_8H_{16} adsorbed per mass of catalyst is assumed to be proportional to its intra-zeolitic concentration. The invariance in the uptake of C_8H_{16} (Figure S16) with Φ_{IR} suggests that the intra-zeolitic concentration of C_8H_{16} in proximity of active sites is not the cause of the difference in epoxidation rates among Ti-BEA. C_8H_{16} likely adsorbs to defect-free regions of the *BEA framework, which nucleate aliphatic-alkene cluster formation and results in nearly-identical C_8H_{16} uptakes among Ti-BEA. Moreover, the rates of epoxidation are highest on hydrophilic Ti-BEA, which, on average, possess greater numbers of $(SiOH)_4$ near Ti active sites than their hydrophobic analogues. As such, it seems unlikely that the concentration of C_8H_{16} (i.e., a hydrophobic reactant) would be a factor of 100 greater near active sites in a hydrophilic environment.

References:

1. Prodinger, S.; Shi, H.; Eckstein, S.; Hu, J. Z.; Olarte, M. V.; Camaioni, D. M.; Derewinski, M. A.; Lercher, J. A., Stability of Zeolites in Aqueous Phase Reactions. *Chem. Mater.* **2017,** *29*, 7255-7262.
2. Prodinger, S.; Derewinski, M. A.; Vjunov, A.; Burton, S. D.; Arslan, I.; Lercher, J. A., Improving Stability of Zeolites in Aqueous Phase via Selective Removal of Structural Defects. *J. Am. Chem. Soc.* **2016,** *138* (13), 4408-4415.
3. Perez-Pariente, J.; Sanz, J.; Fornes, V.; Corma, A., 29Si and 27Al MAS NMR Study of Zeolite Beta with Different Si/Al Ratios. *J. Catal.* **1990,** *124*, 217-223.
4. Fawcett, W. R.; Liu, G.; Kessler, T. E., Solvent-Induced Frequency Shifts in the Infrared Spectrum of Acetonitrile in Organic Solvents. *J. Phys. Chem.* **1993,** *97*, 9293-9298.
5. Pelmenschikov, A. G.; van Santen, R. A.; Jänchen, J.; Meijer, E., CD3CN as a Probe of Lewis and Bronsted Acidity of Zeolites. *J. Phys. Chem.* **1993,** *97*, 11071-11074.
6. Campbell, C. T.; Sellers, J. R., The entropies of adsorbed molecules. *J. Am. Chem. Soc.* **2012,** *134* (43), 18109-18115.
7. *CRC Handbook of Chemistry and Physics*. CRC Press: 2012.
8. McQuarrie, D. A., *Statistical Mechanics*. University Science Books: Mill Valley, 2000.
9. Ayala, P. Y.; Schlegel, H. B., Identification and treatment of internal rotation in normal mode vibrational analysis. *J. Chem. Phys.* **1998,** *108*, 2314-2325.
10. Storhoff, B. N.; Lewis, H. C., Organonitrile Complexes of Transition Metals. *Coord. Chem. Rev.* **1977,** *23*, 1-29.
11. Computational Chemistry Comparison and Benchmark DataBase. https://cccbdb.nist.gov/exp2x.asp?casno=75058 (accessed June 1st, 2018).
12. Reedijk, J.; Groeneveld, W. L., Complexes with Ligands Containing Nitrile Groups. *Recueil* **1968,** *87*, 1079-1088.
13. Bregante, D. T.; Flaherty, D. W., Periodic Trends in Olefin Epoxidation over Group IV and V Framework Substituted Zeolite Catalysts: A Kinetic and Spectroscopic Study. *J. Am. Chem. Soc.* **2017,** *139* (20), 6888-6898.
14. Bregante, D. T.; Priyadarshini, P.; Flaherty, D. W., Kinetic and spectroscopic evidence for reaction pathways and intermediates for olefin epoxidation on Nb in * BEA. *J. Catal.* **2017,** *348*, 75-89.
15. Bregante, D. T.; Thornburg, N. E.; Notestein, J. M.; Flaherty, D. W., Consequences of Confinement for Alkene Epoxidation with Hydrogen Peroxide on Highly Dispersed Group 4 and 5 Metal Oxide Catalysts. *ACS Catal.* **2018,** *8*, 2995-3010.
16. Bregante, D. T.; Patel, A. Y.; Johnson, A. M.; Flaherty, D. W., Catalytic Thiophene Oxidation by Groups 4 and 5 Framework-Substituted Zeolites with Hydrogen Peroxide: Mechanistic and Spectroscopic Evidence for the Effects of Metal Lewis Acidity and Solvent Lewis Basicity. *J. Catal.* **2018,** *364*, 415-425.